



## Green Synthesis of Water Splitting Electrocatalysts: IrO<sub>2</sub> Nanocages via Pearson's Chemistry

Marine Elmaalouf, Alexandre Da Silva, Silvia Duran, Cédric Tard, Miguel Comesaña-Hermo, Sarra Gam-Derouich, Valérie Briois, Damien Alloyeau, Marion Giraud, Jean-Yves Piquemal, et al.

### ► To cite this version:

Marine Elmaalouf, Alexandre Da Silva, Silvia Duran, Cédric Tard, Miguel Comesaña-Hermo, et al.. Green Synthesis of Water Splitting Electrocatalysts: IrO<sub>2</sub> Nanocages via Pearson's Chemistry. Chemical Science, 2022, 13 (40), pp.11807-11816. 10.1039/D2SC03640A . hal-03788367

**HAL Id: hal-03788367**

**<https://hal.science/hal-03788367>**

Submitted on 26 Sep 2022

**HAL** is a multi-disciplinary open access archive for the deposit and dissemination of scientific research documents, whether they are published or not. The documents may come from teaching and research institutions in France or abroad, or from public or private research centers.

L'archive ouverte pluridisciplinaire **HAL**, est destinée au dépôt et à la diffusion de documents scientifiques de niveau recherche, publiés ou non, émanant des établissements d'enseignement et de recherche français ou étrangers, des laboratoires publics ou privés.

# Green Synthesis of Water Splitting Electrocatalysts: IrO<sub>2</sub> Nanocages via Pearson's Chemistry

Marine Elmaalouf,<sup>a</sup> Alexandre Da Silva,<sup>a</sup> Silvia Duran,<sup>b</sup> Cédric Tard,<sup>b</sup> Miguel Comesaña-Hermo,<sup>a</sup> Sarra Gam-Derouich,<sup>a</sup> Valérie Briois,<sup>c</sup> Damien Alloyeau,<sup>d</sup> Marion Giraud,<sup>a</sup> Jean-Yves Piquemal\*<sup>a</sup> and Jennifer Peron\*<sup>a</sup>

Highly porous iridium oxide structures are particularly well-suited for the preparation of porous catalyst layers needed in proton exchange membrane water electrolyzers. Herein, we report the formation of iridium oxide nanostructured cages, via a water-based process performed at room temperature, using cheap Cu<sub>2</sub>O cubes as template. In this synthetic approach, based on Pearson's hard and soft acid-base theory, the replacement of the Cu<sub>2</sub>O core by an iridium shell is permitted by the difference in hardness/softness of cations and anions of the two reactants Cu<sub>2</sub>O and IrCl<sub>3</sub>. Calcination followed by acid leaching allow the removal of residual copper oxide cores and leave IrO<sub>2</sub> hierarchical porous structures with outstanding activity toward the oxygen evolution reaction. Fundamental understanding of the reaction steps and identification of the intermediates are permitted by coupling a set of *ex situ* and *in situ* techniques including *operando* time-resolved X-ray absorption spectroscopy during the synthesis.

## 1. Introduction

Iridium oxide ( $\text{IrO}_2$ ) is the only electrocatalyst being active toward the oxygen evolution reaction (OER) and sufficiently stable to sustain the harsh conditions, highly oxidative and strongly acidic, existing at the anodes of proton exchange membrane water electrolysis (PEMWE) cells. For this reason and despite extensive research,  $\text{IrO}_2$  is still the catalyst used in commercial devices, with loading contents approaching  $2 \text{ mg cm}^{-2}$ .<sup>1,2</sup> Nevertheless, due to its scarcity and high cost, its loading needs to be decreased while its activity and stability should be at least maintained and if possible, improved. The decrease in catalyst loading can be attained either by increasing the intrinsic activity of the catalysts by, for instance, modifying its composition (usually at the expense of its stability); or by preparing materials with extensive and accessible surface areas for the catalytic reaction. It is noteworthy that the use of electron conducting catalyst supports, such as high surface area carbons, is also prevented by the highly oxidative environment. Meanwhile, porosity is of the outermost importance given the necessity for high gas and water transport capabilities.

Porous  $\text{IrO}_2$  thin films have shown promising properties.<sup>3, 4</sup> However, while providing proof of performances and stability enhancement through a fine control of the material's architecture, these methods are difficult to scale up and cannot be easily used to prepare porous catalyst layers to be deposited on the membrane and transferred into devices.

Hollow noble metal nanocatalysts can be fabricated *via* galvanic replacement,<sup>5-9</sup> Kirkendall effect, dealloying and selective etching.<sup>10, 11</sup> Moreover, decreasing the noble metal content can be achieved by developing thin layers in the form of either core@shell or hollow nanoparticles. So-called Extended Surface Area (ESA) catalysts comprise large metal surfaces extended in two dimensions like thin films,<sup>5</sup> the high density of atomic steps and kinks providing more active sites for the catalytic reaction to occur. Electronic and/or strain effects caused by foreign atoms located in the inner layer or partially alloyed with the skin-catalyst particles are responsible for enhanced performance since they modify the chemisorption and reactivity of intermediates at the surface.<sup>12-14</sup> These particular structures have shown to be beneficial in fuel cells by making catalysts more resistant to surface area loss, providing long range conductivity and reduced mass transport losses.<sup>15</sup>

While these strategies have been widely applied in the past few years for fuel cells, only a few papers have been reported on the preparation of hollow Ir-based catalysts.<sup>16-18</sup> Ir-Ni@ $\text{IrO}_x$  core-shell NPs were prepared from  $\text{IrNi}_x$  alloys by electrochemical Ni leaching and concomitant Ir oxidation<sup>18</sup>, while dodecahedral IrNi nanoframes were obtained using lanthanide metal-assisted

synthesis.<sup>19</sup> Nanosegregation was also used to displace Ir at the surface of an IrFe alloy after thermal treatment under  $\text{H}_2/\text{Ar}$ ,<sup>20</sup> or at the surface of IrRu alloys.<sup>21</sup> PdIr bimetallic octapods and nanocages were obtained by using Pd nanocubes as sacrificial template and subsequent co-reduction using a polyol (EG) with an Ir precursor.<sup>22</sup> Cobalt-doped IrCu octahedral nanocages showed lower overpotential compared to Ir/C nanocatalysts (0.293 vs. 0.315 V @  $10 \text{ mA cm}^{-2}$ ) and excellent stability.<sup>17</sup> Based on a modified galvanic replacement, Cu nanoparticles were used as template to prepare single-crystalline CuIr polyhedral nanocages at  $250^\circ\text{C}$ . CuIr nanocrystals were obtained by the co-decomposition of Cu and Ir precursors at high temperature in oleylamine under CO atmosphere.<sup>23</sup> More recently, Cu@Ir core-shell particles were obtained in diphenylether/oleylamine.<sup>24</sup> For obvious environmental and economic reasons, water-based syntheses are strongly preferable. By using water as the synthesis medium taking advantage of the aerosol process, we have also recently reported the preparation of highly porous  $\text{IrO}_2$  and Ir-based mixed oxides and alloys catalysts from polymeric templates.<sup>25-27</sup>

Regarding water-based solution synthesis, the coordinating etching and precipitating (CEP) mechanism has been reported in the literature for the direct formation of porous oxides,<sup>28</sup> e.g. for producing  $\text{SnO}_2$  boxes for lithium battery anodes with high lithium storage capacity.<sup>29</sup> This strategy inspired by Pearson's hard and soft acid-base concept (HSAB) has been applied for the production of hollow nanostructures of several transition metal oxides based on Fe,<sup>30-32</sup> Co,<sup>30-34</sup> Ni,<sup>30, 31, 35, 36</sup> Zn,<sup>31</sup> Mn,<sup>31</sup> Sn,<sup>29</sup> and Ti.<sup>37</sup> To the best of our knowledge, this approach has never been implemented for the formation of noble metal-based oxides. In CEP syntheses, water or water/alcohol solutions are used as the synthetic medium and,  $\text{Cu}_2\text{O}$  nanostructures are typically used as templates because they are cheap, easy to synthesize and offer a wide variety of morphologies.<sup>28, 38</sup>  $\text{S}_2\text{O}_3^{2-}$  or  $\text{Cl}^-$  ions are in general added in the reaction medium to facilitate the displacement towards  $\text{Cu}_2\text{O}$  dissolution, and the reactions are performed in water/alcohol solution to control precursor hydrolysis and, as a consequence, the kinetics of the reaction. Nevertheless, this strategy has not been applied to produce hollow structures of noble metals since most of their cations are known to be soft acids, *i.e.* have comparable softness with Cu(I) ions, and therefore are not suitable for this replacement. Since Ir(III) ions present a harder character than other noble metals cations, they should permit hollow oxides to be obtained through CEP.<sup>39</sup> In this work, we extend this original strategy, performed in water and at room temperature, to obtain hollow  $\text{IrO}_2$  nanocages in a three step process, by using  $\text{Cu}_2\text{O}$  nanocubes as sacrificial templates (Figure 1). In the first step,  $\text{IrCl}_3$  reacts with  $\text{Cu}_2\text{O}$  nanocubes to form a yolk shell structure in which precipitated Ir species surround a residual  $\text{Cu}_x\text{O}$  core. Subsequent calcination in air and acid leaching allow producing nanocages consisting of small isotropic  $\text{IrO}_2$  nanoparticles that are highly active towards the OER. Besides producing highly porous architectures from cheap templates, this synthesis strategy is environmentally friendly since it is performed in water at room temperature.

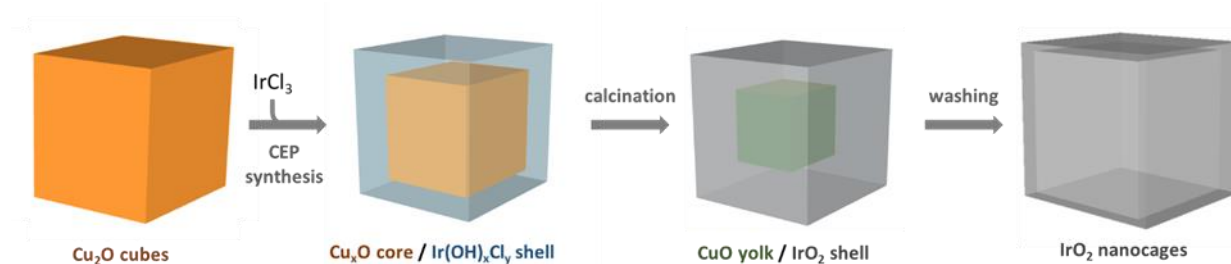


**Figure 1.** Schematic representation of the 3-steps formation of IrO<sub>2</sub> nanocages from Cu<sub>2</sub>O templates.

## 2. Results and Discussion

**CEP synthesis of hydrous iridium hollow structures.** According to Pearson's table,<sup>39</sup> Cu<sup>+</sup> ions present in Cu<sub>2</sub>O show a softer character than Ir<sup>3+</sup> ions (classified as "borderline") while O<sup>2-</sup> is harder than Cl<sup>-</sup>. For this reason, when Cu<sub>2</sub>O nanoparticles interact with an aqueous solution of IrCl<sub>3</sub>, Cu<sup>+</sup> ions will progressively be released to interact

with Cl<sup>-</sup> ions. Being unstable in aqueous solution, Cu<sup>+</sup> will also be rapidly oxidized into Cu<sup>2+</sup>.<sup>40</sup> As the Cu<sub>2</sub>O particles will dissolve, Ir<sup>3+</sup> will interact with OH<sup>-</sup> species resulting from the dissolution of Cu<sub>2</sub>O. Following a CEP mechanism, and given that the appropriate conditions are met, Ir(OH)<sub>x</sub> species will precipitate as soon as they form, leading to the replacement of the initial Cu<sub>2</sub>O nanocubes by Ir(OH)<sub>x</sub> nanocages.

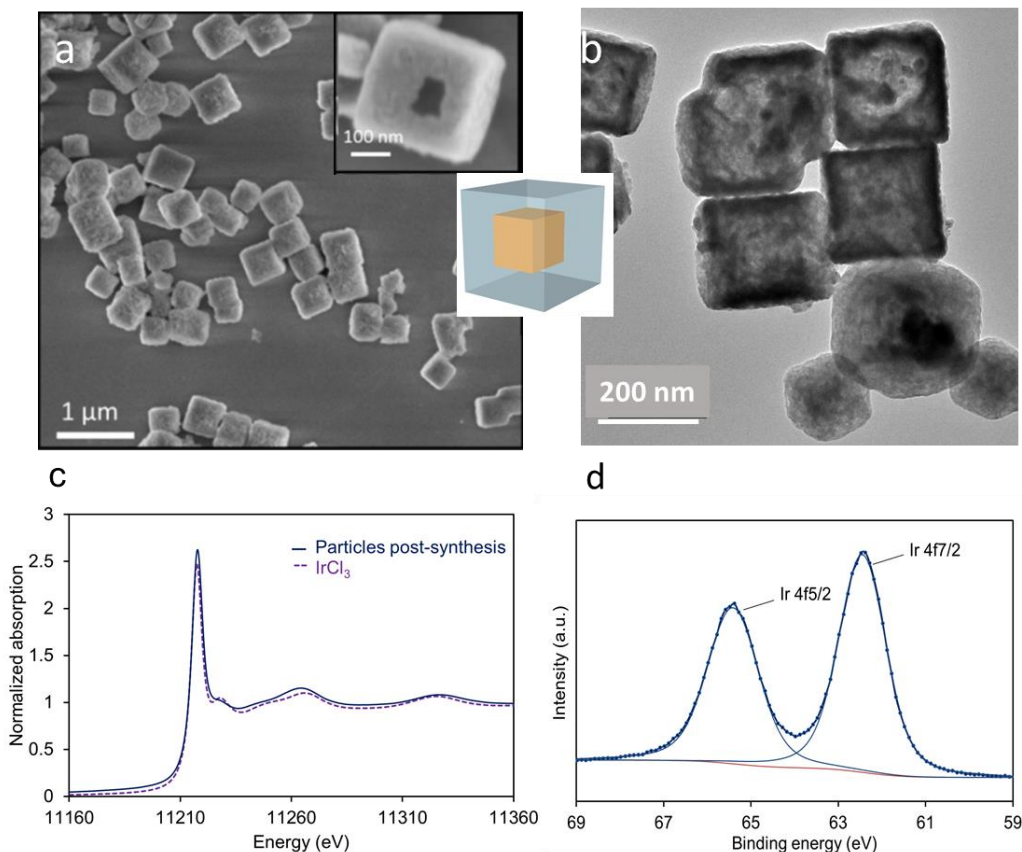


**Figure 2.** (a) SEM and (b) TEM images of the particles recovered after synthesis. (c) Ir L<sub>3</sub> XANES spectrum of the particles recovered after synthesis and of the precursor IrCl<sub>3</sub>. (d) XPS spectrum in the Ir 4f region of the particles recovered after synthesis.

To perform such synthesis, Cu<sub>2</sub>O cubes reacted with IrCl<sub>3</sub>, while using polyvinylpyrrolidone (PVP) to prevent the aggregation of the particles. The Cu<sub>2</sub>O microparticles used as template hold a cubic cuprite structure with space group Pn-3m as confirmed by XRD measurements (Figure S1). After 20 h of reaction, hollow structures

preserving the original morphology of the initial Cu<sub>2</sub>O cubes are obtained (Figure 2a). We observe a 20% decrease in particle size from the initial *ca.* 320 nm edge length of the Cu<sub>2</sub>O cubes to the final 265 nm ( $\sigma = 6\%$ ) after CEP treatment. XRD analysis of the materials recovered after synthesis by centrifugation show a very

broad peak centered around 35° characteristic of an amorphous phase, as well as several residual peaks characteristic of the initial Cu<sub>2</sub>O template (Figure S1). X-ray photoelectron spectroscopy (XPS) analysis of the Cu species reveals the presence of mostly Cu(II) with a ratio Cu(I)/Cu(II) of 5/95 (Figure S2). Transmission electron microscopy (TEM) analyses show that the cages are made of a dense shell and a residual and more diffuse core that is unstable under the electron beam (Figure 2b). The Ir/(Ir+Cu) ratios obtained from scanning electron microscopy with energy dispersive X-ray analysis (SEM-EDX) and X-ray fluorescence (XRF) show that Ir represents *ca.* 20% of the total metal content in the resulting nanocage (Table 1).

**Table 1.** Ir content in the particles recovered after synthesis. Standard deviations were calculated on four different samples for XRF and in five different zones of one sample for SEM-EDX analysis.

	XRF	SEM-EDX	XPS
$\left(\frac{Ir}{Cu+Ir}\right) \%, (SD)$	19 (1.4)	18 (5.2)	26

The slightly higher amount of Ir detected by XPS, a surface sensitive technique, indicates that a higher amount of Ir is located on the surface of the nanocages. We can conclude that after the CEP reaction, the particles are made of an Ir-rich shell surrounding a residual core mostly made of hydrated Cu(II) species.

To discard a galvanic reaction between Ir<sup>3+</sup> and Cu<sup>+</sup>, and confirm a CEP mechanism, we have analyzed the oxidation state of Ir after reaction using X-ray absorption spectroscopy (XAS) and XPS (spectra in Figure 2c and d, respectively). The XPS spectra obtained after CEP synthesis show the presence of only two peaks centered at 62.4 and 65.4 eV, corresponding to Ir 4f<sub>7/2</sub> and Ir 4f<sub>5/2</sub> signals from Ir(III). The absence of signatures at 60.9 eV and 63.9 eV indicate the absence of Ir(0) at the surface of the sample. The peak top position of the XANES spectra recorded at the Ir L<sub>3</sub>-edge on post-synthesis material is measured at 11218 eV and confirms the presence of Ir(III). The absence of Ir(0) discards a replacement through a galvanic reaction. This finding is a very important point since in the case of Pt for instance, Hong *et al.*<sup>41</sup> have shown that they are able to produce noble metal hollow structures from Cu<sub>2</sub>O templates, but in their case, the resulting material is made of a PtCu alloy hence results from a redox reaction between Pt and Cu cations. In the current mechanism, while Cu(I) is prone to oxidation in water, the transformation of Cu(I) into Cu(II) species does not induce Ir(III) reduction.

**In situ and ex situ study of the reaction kinetics.** Several parameters had to be adjusted to allow for the formation of the

hollow structure. Indeed, kinetics of both dissolution and precipitation processes have to be synchronous to preserve the template morphology and the Ir-based shell has to coat uniformly the surface of the template. PVP was needed in order to obtain well separated nanocubes. Unlike for syntheses performed with transition metals cations, the duration of the experiment in the case of Ir was found to be relatively long, *ca.* 20 h. Materials obtained at higher temperatures (30 °C or 60 °C) are made of IrO<sub>2</sub> particles that precipitate separately from the cubes (Figure S3), while higher IrCl<sub>3</sub> concentration (Ir/Cu 1.5 vs. Ir/Cl 0.5 in optimal conditions) leads to very fast dissolution of Cu<sub>2</sub>O cubes without precipitation of Ir species.

To get better insight into the mechanisms of formation of these hollow structures, the replacement reaction was followed both by *ex situ* techniques analyzing the particles after different reaction times (SEM-EDX) and by *in situ* quick-XAS recorded simultaneously at both edges on the same solution. SEM images of the particles recovered after 1 h, 3 h, 8 h, 20 h, and 40 h of reaction are displayed in Figure 3a. Corresponding Ir content compared to total metal content obtained from EDX analysis is plotted as a function of reaction time on Figure 3b. After 1 h of reaction, we can already see that the surface of the Cu<sub>2</sub>O cubes becomes slightly rough, while no Ir can be detected. After 3 h, the surface roughness is more pronounced and the Ir/(Ir+Cu) ratio detected in the cubes is 3%. As the reaction proceeds, the iridium content in the particle increases to reach a plateau of *ca.* 18 at.% of Ir after 15 h. Subsequently, the surface recovers a smoother texture while internal voids are observed either from broken particles or by contrast arising from SEM in *in lens* imaging mode. The amount of Ir detected by EDX agrees with XRF analysis of the powder recovered after synthesis. Interestingly, the profile of Cl content, determined from EDX measurements (Figure 3b) in the material follows that of Ir. To determine the nature of the precipitated Ir species, the final material recovered by centrifugation was analysed by XAS. Fourier transform (FT) of the Ir L<sub>3</sub>-edge EXAFS spectra for the sample obtained after synthesis is plotted in Figure 3c along with those of IrCl<sub>3</sub> in aqueous solution and IrO<sub>2</sub> as pellet used as reference. On the FT-EXAFS spectra of IrCl<sub>3</sub>, one peak characteristic of Ir-Cl distances is observed at R' = 1.99 Å (uncorrected for phase shift). On the FT-EXAFS spectra of IrO<sub>2</sub>, the Ir-O characteristic peak is observed at R' = 1.65 Å, while further Ir-Ir distances are observed at *ca.* 3 and 3.5 Å.<sup>27</sup> Two contributions can be clearly observed in the CEP sample, one arising from Ir-Cl distances and a shoulder located at a shorter radial distance and characteristic of Ir-OH distances. From EXAFS fitting, the average number of Cl and OH neighbors can be determined; Ir(III) species are coordinated both with Cl and OH groups to form an Ir(OH)<sub>2</sub>Cl<sub>4</sub> first coordination shell (Figure S4, Table S1). A Cl/Ir ratio of *ca.* 4 obtained from SEM-EDX is in agreement with this formula (Figure S5).

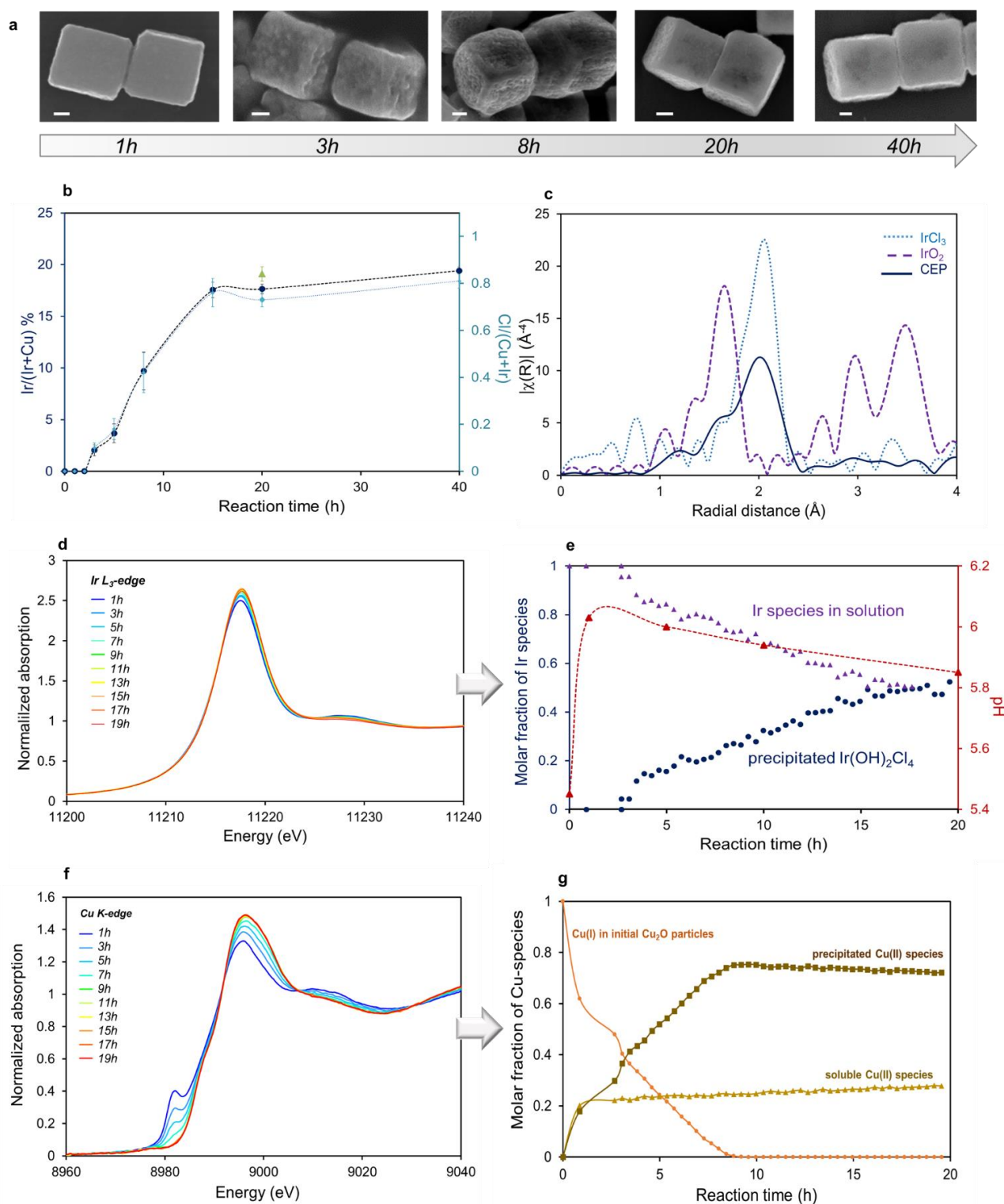


**Figure 3.** (a) SEM images of the particles recovered after different reaction time (scale bars: 100 nm) and (b) corresponding EDX analysis of Ir and Cl content (SD error bars calculated in 3 different areas including several and/or isolated particles). (c) FT-EXAFS spectra of the particles after synthesis (labeled CEP), IrCl<sub>3</sub> and IrO<sub>2</sub> as references. (d) XANES spectra at the Ir L<sub>3</sub>-edge recorded *in situ* as a function of reaction time and (e) molar fraction of precipitated Ir species and of soluble Ir(III) species in solution (violet triangles) determined by MCR-ALS from *in situ* XAS measurements (blue circles), and pH evolution as a function of time of reaction (red triangles). (f) XANES spectra at the Cu K-edge recorded *in situ* as a function of reaction time and (g) molar fraction of Cu species determined by MCR-ALS from *in situ* XAS measurements: initial cubes in orange circles, soluble Cu(II) species in light green triangles, precipitated amorphous Cu(II) species in olive squares.

The evolution of the different Ir and Cu species along the same reaction was also followed *in situ* by quick-XAS in a

polyetheretherketone (PEEK) cell. XANES spectra recorded at the Ir L<sub>3</sub>-edge and Cu K-edge and evolution of Ir and Cu molar fractions

determined using multivariate curve resolution analysis (MCR-ALS) of the normalized XAS spectra as a function of reaction time are represented in Figure 3d-g. Experimental details on MCR-ALS analysis for Ir and Cu are provided in Figure S6 and S7, respectively. We can observe in Figure 3d that the rising edge position and the maximum of the white line of the XANES spectra do not vary with reaction time, confirming that Ir keeps its oxidation state (III) along the reaction. EXAFS fitting confirms that the Cl precursor evolves into a precipitated  $\text{Ir}(\text{OH})_2\text{Cl}_4$  species. The evolution of the molar fraction of  $\text{Ir}(\text{OH})_2\text{Cl}_4$  relative to total Ir species along the 20 h of reaction is shown in Figure 3e. After an induction period of 3 h, similar to what was observed by SEM-EDX analysis, the molar fraction of  $\text{Ir}(\text{OH})_2\text{Cl}_4$  in the reaction medium increases to *ca.* 45% after 20 h. These results indicate that 45% of the iridium initially introduced in the reaction medium reacts to form  $\text{Ir}(\text{OH})_2\text{Cl}_4$ . This value is in agreement with the one determined by X-ray fluorescence (XRF) analysis of both the supernatants and the particles obtained after 20 h. From these measurements we obtain a conversion rate of Ir into deposited species of 33.8% ( $\sigma = 12.4\%$  calculated from 4 different reaction batches).  $\text{Ir}(\text{OH})_2\text{Cl}_4$  precipitates at the surface of residual copper oxide particles leading to a final  $\text{Ir}/(\text{Ir}+\text{Cu})$  ratio of *ca.* 20%.

From MCR-ALS analysis applied to the series of XAS spectra recorded at the Cu K-edge (Figure 3f) we can see that the initial  $\text{Cu}_2\text{O}$  is converted into two different species (Figure 3g). Part of  $\text{Cu}_2\text{O}$  (*ca.* 30-40%) quickly dissolves into soluble  $\text{Cu}(\text{H}_2\text{O})_6^{2+}$  species. The remaining copper species (60-70%) arises from the evolution of solid state  $\text{Cu}_2\text{O}$  into amorphous Cu(II)-based solid in which Cu(II) ions are surrounded by 4 oxygen atoms, as determined by the fitting of the EXAFS spectra of the particles recovered after synthesis (Figure S8, Table S2). These results seem to indicate that 60% of the initial Cu atoms remain in the final particles. Indeed, this calculation is confirmed by XRF analysis of both the supernatants and the particles obtained after 20 h of reaction. From these measurements we found that 42.6 % ( $\sigma = 14.4\%$ ) of Cu atoms are dissolved and recovered in the supernatant.

The plateau in Ir content in the final objects (Figure 3b), equivalent to a maximal conversion rate, could possibly be attributed to the sluggish outwards diffusion of Cu atoms after the deposition of a certain amount of Ir species at the surface. Another explanation could be related to a restricted pH range in which the formation and precipitation of  $\text{Ir}(\text{OH})_2\text{Cl}_4$  species is possible. Accordingly, the pH of the solution was followed along the course of the experiment (Figure 3e). We can see that the initial pH is slightly acidic due to the dissolution of the Ir precursor, followed by a progressive increase during the first 2.5 h of the reaction until reaching a value of *ca.* 6.1. After approximately 8 h, the pH starts to decrease, and by the end of the reaction (20 h) it reaches 5.8.

**Mechanism of the reaction.** All these observations have allowed us to propose a mechanism to explain the replacement reaction of  $\text{Cu}_2\text{O}$  nanocubes into Ir-based nanocages that is schematized in Figure 4. In a first step, the slightly acidic pH induces partial dissolution of  $\text{Cu}_2\text{O}$  cubes into Cu(I) species that are very quickly oxidized into soluble Cu(II) species and  $\text{OH}^-$ . Indeed, Cu(I) in aqueous solution is not stable and rapidly oxidizes into Cu(II).<sup>40</sup> Within the first 3 h, the pH increases due to the release of  $\text{OH}^-$ , leading to an induction period in which no Ir is detected at the surface of the particles. Released  $\text{OH}^-$  react with the  $\text{IrCl}_3$  to form  $\text{Ir}(\text{OH})_2\text{Cl}_4$ , species that precipitate when a sufficiently high pH is reached. According to the Pourbaix diagram, when the pH increases above 5-6, the precipitation of  $\text{Cu}(\text{OH})_2$  is favored at the expense of soluble Cu(II) species. This explains why the amount of soluble Cu(II) ions quickly stabilizes at *ca.* 30% of the total Cu content (Figure 3g). Subsequently,  $\text{Cu}_2\text{O}$  is further transformed into amorphous  $\text{Cu}(\text{OH})_2$  solid phase within the particle when the pH of the solution is high enough. Even though the solubility of  $\text{Cu}(\text{OH})_2$  is very low, the equilibrium established between solid  $\text{Cu}(\text{OH})_2$  and soluble Cu(II) species at this pH range allows the outwards diffusion of  $\text{OH}^-$ . The latter species immediately react with Ir precursors, producing the precipitation of a thicker  $\text{Ir}(\text{OH})_x\text{Cl}_2$  layer that leads to a smoother particle's surface. Such reaction occurs until the diffusion of  $\text{OH}^-$  is impeded by the precipitated layer of  $\text{Ir}(\text{OH})_2\text{Cl}_4$  and/or until the pH becomes too low to allow the formation of the hydroxylated Ir complex.



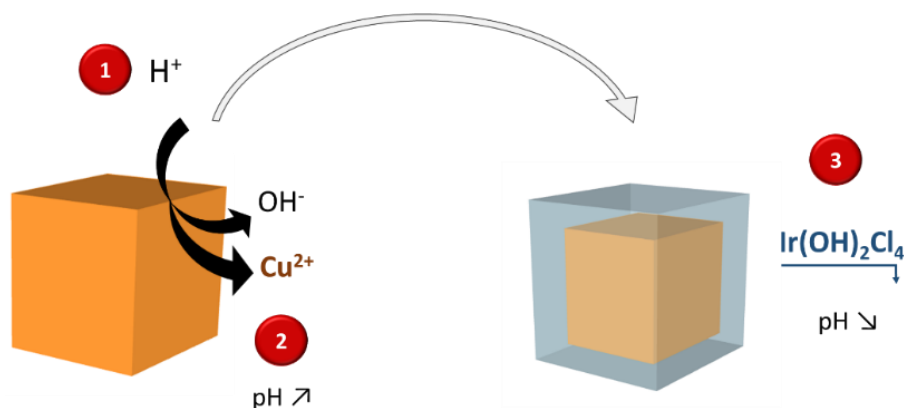


**Figure 4.** Schematic representation of the CEP mechanism for the formation of  $\text{Ir(OH)}_x\text{Cl}_y$  from  $\text{Cu}_2\text{O}$  templates. Step 1: dissolution of  $\text{Cu}_2\text{O}$  cubes and release of  $\text{Cu}^{2+}$  and  $\text{OH}^-$ . Step 2: pH increases due to the release of  $\text{OH}^-$ . Step 3: the  $\text{Ir(OH)}_2\text{Cl}_4$  forms and precipitate while  $\text{OH}^-$  is consumed and the pH decreases.

**Calcination.** The Ir-based particles obtained after synthesis were calcined to convert the hydroxylated species into crystalline  $\text{IrO}_2$  nanoparticles. Subsequently, the activity of the calcined material towards the water oxidation in acidic conditions was evaluated in a three-electrode electrochemical setup. Indeed,  $\text{IrO}_2$  is the gold-standard catalyst for OER in acidic media due to its unmatched activity and stability. However, for such purpose, the calcination temperature to convert the Ir precursor into  $\text{IrO}_2$  is of high importance since it is well known that amorphous iridium oxide materials or materials with very small crystallite size show higher electrochemical activity than their well-crystallized counterparts.<sup>25, 42, 43</sup> The optimal calcination temperature usually ranges between 400 °C and 500 °C, where the crystallisation of rutile  $\text{IrO}_2$  occurs. Lower calcination temperature leads to unstable materials and higher one to larger crystals and lower activity.<sup>26, 44</sup>

To convert hydroxylated Ir species into  $\text{IrO}_2$ , the as-synthesized materials were further calcined from 400 to 550 °C for 15 min in a muffle furnace. X-ray diffractograms and corresponding crystallite size are reported in Figure S9. We can see from XRD analysis that the material starts to crystallize above 400 °C. At 450 °C and above, peaks characteristic of  $\text{IrO}_2$  are detected along with  $\text{CuO}$  peaks. Indeed, the residual amorphous Cu-containing phase is converted into the thermally-stable phase of  $\text{CuO}$  at 450 °C, leading to sharper peaks as the crystallite size increases with calcination temperature. At 450 °C we observe the appearance of  $\text{IrO}_2$  diffractions, coming from crystallites with sizes below 2 nm. These objects increase to 2.3 nm then 2.8 nm when the temperature is increased to 500 °C and 550 °C, respectively.  $\text{CuO}$  crystallites are much larger and increase from 23 nm to 36 nm when the calcination temperature is increased from 450 °C to 550 °C. TEM images reveal a yolk shell structure in which small  $\text{IrO}_2$  isotropic nanoparticles constitute the shell and large  $\text{CuO}$  particles are present in the internal void (Figure S10).

Subsequently, the particles were washed with HCl solution to remove the non-noble metal oxide core and increase the inner porosity of the nanocages. Typical objects obtained after

calcination at 550 °C and washed with acid are presented in Figure 5. XRD confirms the disappearance of the  $\text{CuO}$  phase (Figure S11) and SEM and TEM images show hollow particles with a well-maintained morphology. While  $\text{CuO}$  is not detected anymore by XRD, XRF of the washed particle give a residual Cu content of *ca.* 4 wt.%. Electron diffraction obtained from HR-TEM images leads to an inter-planar distance of 3.25 Å (Figure 5d) which is slightly larger than the theoretical value corresponding to (110) planes found in bulk  $\text{IrO}_2$  (3.18 Å). Such difference is probably due to the lattice expansion induced by the small particle size.<sup>45</sup>

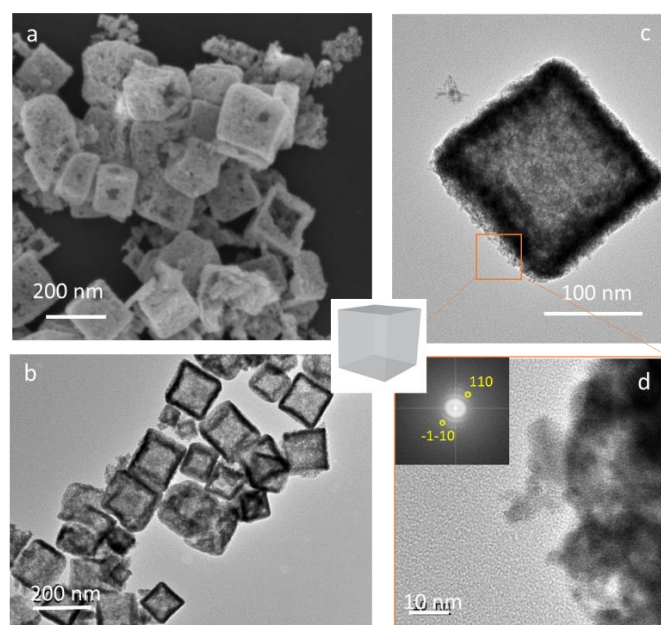


**Figure 5.** (a) SEM, (b-c) TEM and (d) HR-TEM images of the particles recovered after synthesis, calcined at 550 °C and acid leached. The inset in (d) corresponds to the Fourier transform of the image on which the inter-reticular distances can be measured.



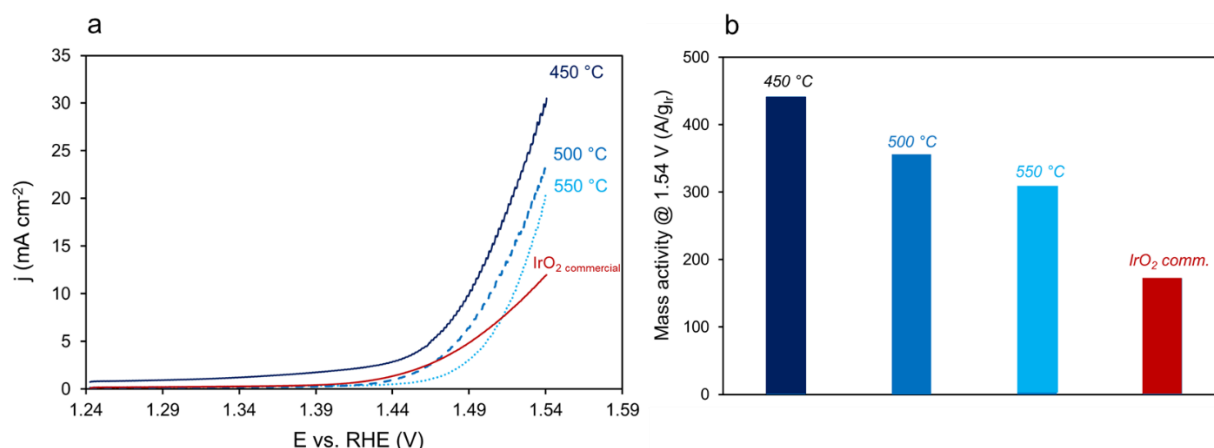


**Figure 6.** (a) IV curves of the samples calcined at 450 °C, 500 °C and 550 °C and commercial IrO<sub>2</sub> and, (b) corresponding mass activities measured at 1.54 V and calculated using the actual mass of Ir in each sample. Experiments performed in H<sub>2</sub>SO<sub>4</sub> 0.05 M with a scan rate of 10 mV s<sup>-1</sup> after conditioning (50 cycles between -0.2 and 1.2 V vs SHE at 200 mV s<sup>-1</sup>). Surface area of the electrode: 0.196 cm<sup>2</sup>, total catalyst loading: 16 µg.

#### Activity of the nanocages towards the Oxygen Evolution Reaction.

The electrochemical activity toward the OER of the acid-leached nanocages calcined from 400 °C to 550 °C was evaluated in a three-electrodes electrochemical setup and compared to commercial IrO<sub>2</sub> as a reference. The current densities normalized to the actual mass of iridium is shown in Figure 6a, and the corresponding mass activity determined at 1.54 V in Figure 6b. As expected, the activity decreases when the calcination temperature increases to 500 °C due to crystallization of the materials. Nevertheless, the mass activity of the prepared catalysts is higher than commercial IrO<sub>2</sub> particles, whatever the calcination temperature. The very small size of IrO<sub>2</sub> nanoparticles and the high accessibility to catalytic sites allowed by the highly porous architecture lead to highly active materials. The mass activity of the IrO<sub>2</sub> cages calcined at 450 °C is of 450 A/g<sub>Ir</sub>, *i.e.* more than two times higher than that of commercial IrO<sub>2</sub> particles. The surface area of the catalyst calcined at 550 °C, determined using mercury underpotential deposition, was found to be of 37 m<sup>2</sup> g<sup>-1</sup>.<sup>46</sup>

### 3. Conclusion

In summary, we have developed a new synthetic strategy for the preparation of iridium oxide nanocages from cheap inorganic templates. The water-based synthesis, performed at room temperature, proceeds through a CEP mechanism as evidenced from XPS, SEM, and *in situ* and *ex situ* XAS experiments. Such multi-technique approach allows us to follow the transformation of Cu and Ir species along the reaction. After an induction period during which copper ions start to dissolve, hydroxylated-chlorinated iridium species precipitate at the surface of the cubes, forming a solid shell. After 20 h of reaction, core-shell structures made of Cu species surrounded by an Ir-rich shell are formed. The morphology of the material is well-suited to obtain hierarchical hollow structures in

which ultra-small nanoparticles are assembled into hollow cages. Accordingly, the resulting materials can be easily converted into hollow IrO<sub>2</sub> nanocages, leading to electrocatalytic performances for the OER that are more than two times higher than those obtained with the commercial standard. Further work is ongoing to recycle the synthesis solution and reduce Ir precursor losses during the synthesis.

## 4. Experimental Section

**Synthesis.** IrCl<sub>3</sub>·xH<sub>2</sub>O (98%) and commercial IrO<sub>2</sub> (Premion®) were purchased from Alfa-Aesar. All the other reactants were purchased from Sigma-Aldrich. In a typical synthesis, 90 mg of Cu<sub>2</sub>O cubes are dispersed into 145 mL of mili-Q water along with 1g of PVP (MW: 40000 g mol<sup>-1</sup>). After 1 h of mechanical stirring, 75 mL of a 9.10<sup>-3</sup> M aqueous solution of IrCl<sub>3</sub>·xH<sub>2</sub>O and 30 mL of a 0.43 M NaCl aqueous solution are added to the Cu<sub>2</sub>O/PVP dispersion. The reaction medium is stirred at room temperature for the desired reaction time. The reaction is stopped by centrifugation of the solution at 22000 rpm for 15 min. The particles collected after the first centrifugation are washed twice with a H<sub>2</sub>O/EtOH (250/50 vol./vol.) mixture and once with pure ethanol. The greenish particles are then dried at room temperature under dynamic vacuum overnight. The samples are calcined in a muffle furnace from ambient temperature to the desired temperature with a heating ramp of 15 °C/min, and hold at the maximum temperature for 15 min. The particles are washed with a 0.5 M HCl solution for 15 min. The solution immediately turns dark blue. After 15 min the particles are recovered by centrifugation and washed twice with DI water.

**Scanning Electron Microscopy (SEM).** SEM-EDX experiments were performed on a ZEISS Gemini SEM 360 equipped with an Oxford Instruments Ultim Max 170 mm<sup>2</sup> detector. SEM images and EDX

mapping were obtained by Inlens SE detector (In Column) at 5 kV accelerating voltage. Oxford Instrument AZtec software was used for the acquisition of EDX maps, point & ID analysis. For following the particles along the reaction, aliquots of the synthesis solution were samples after different time of reaction, centrifuged and the collected particles were dispersed in ethanol and deposited on silicon wafers and dried in air.

**Transmission electron microscopy (TEM).** TEM images were obtained using a JEOL 2100 Plus transmission electron microscope operating at an acceleration voltage of 200 kV. Samples were prepared by depositing a drop of a diluted suspension of the nanoparticles in ethanol on a carbon-coated Cu grid.

**X-ray Diffraction (XRD).** XRD measurements were carried out using a Panalytical X'pert pro diffractometer equipped with a Co anode ( $\lambda_{\text{Co}} = 1.79031 \text{ \AA}$ ) and a multichannel X'celerator detector. All the diffractograms were fitted via MAUD program (Material Analysis Using Diffraction), a general X-ray diffraction program based mainly on the Rietveld refinement method,<sup>47</sup> and allowing determination of  $a$  and  $c$  parameters as well as the calculated crystallites sizes for each diffraction peak.

**Energy Dispersive X-ray Fluorescence (EDXRF).** Elemental analyses of the powders were conducted by Energy Dispersive X-ray Fluorescence (EDXRF) using an epsilon 3XL spectrometer from Panalytical equipped with a silver X-ray tube. The calibration was performed by depositing a mass in the range 5-20  $\mu\text{g}$  of the standard solution of each element on a polycarbonate membrane. The same conditions were adopted for all samples. The detection limits for Cu and Ir were determined to be 10 and 12 ng, respectively.

**X-ray photoelectron spectroscopy (XPS).** XPS spectra were recorded using a K-Alpha+ spectrometer from ThermoFisher Scientific, fitted with a microfocused, monochromatic Al  $K_{\alpha}$  X-ray source ( $h\nu = 1486.6 \text{ eV}$ ; spot size = 400 micrometers). The pass energy was set at 150 and 40 eV for the survey and the narrow regions, respectively. Spectral calibration was determined by setting the main C1s (C-C, C-H) component at 285 eV.

**Electrochemical characterization (OER protocol).** The potentiostat used for cyclic voltammetry was an Autolab PGSTAT 12, and ohmic drop was compensated in all cases (typically 30  $\Omega$ ). The working electrode was a 5 mm diameter glassy carbon rotating disk electrode (Pine Instrument), carefully polished and ultrasonically rinsed in absolute ethanol before use. The counter electrode was a platinum wire and the reference electrode an aqueous saturated calomel electrode. All experiments were carried out in air at 10 mV/s and at a rotating rate of 1600 rpm. A 0.05 mol.L<sup>-1</sup> sulfuric acid solution (sulfuric acid, 0.1 N standardized solution, Alfa Aesar) was used as supporting electrolyte. From a mixture of 1 mg of synthesized material or iridium oxide (99.99 %, Alfa Aesar), 2 mg of carbon Vulcan XC72R (Cabot), 250  $\mu\text{L}$  of Nafion solution (5 % w/w, Alfa Aesar) and 250  $\mu\text{L}$  of deionized water (0.059  $\mu\text{S cm}^{-2}$ ), 8  $\mu\text{L}$  of this suspension were deposited on the electrode surface, which was then dried in air and left for 30 min at 60 °C in an oven. Catalysts were then submitted

to 50 cycles between -0.2 and 1.2 V at 200 mV s<sup>-1</sup>, and the 50th forward scan recorded at 10 mV/s in 0.05 M H<sub>2</sub>SO<sub>4</sub> is presented.

**XAS/Quick-XAS.** Cu K-edge and Ir L<sub>3</sub>-edge X-ray absorption spectra were collected in the time-resolved Quick-XAS mode at the ROCK beamline (Synchrotron SOLEIL)<sup>48</sup> at a storage ring energy of 2.75 GeV and a nominal current of 500 mA. XAS measurements were carried out using the edge jumping capability of the Quick-XAS Si(111) channel-cut monochromator which allow to alternate measurements at both edges every 5 min with change of the Bragg angle of the monochromator and optimization of the stripes of harmonic rejection mirrors set at 2.8 mrad of grazing incidence. At the Cu K edge, B4C stripes were used whereas Pd ones were selected for harmonic rejection at the Ir L<sub>3</sub> edge. The frequency of oscillations of the monochromator was 2 Hz enabling to record a single XAS spectrum in 250 ms. For the whole measurements, XAS spectra were measured in transmission mode with three ionization chambers (IC) filled with nitrogen as X-ray detectors. Reference samples were measured either as pellets in boron nitride (15-20% wt. for Ir-based species and 3-4 wt.% for Cu-based species) or as 20 mM aqueous dispersion or solution (based on metal content). Solution samples and *in situ* experiments were carried out in air, in homemade PEEK cells with an optical path of 6 mm. The conditions for the *in situ* experiments were similar to the synthesis conditions except that the reaction volume was reduced to *ca.* 2-2.5 mL. The concentrations were rather low and absorption edges intensities were below 0.1 for the two elements. In order to improve the S/N ratio, 600 spectra recorded consecutively with ascending Bragg angles were merged at each edge during the monitoring of the reaction. The reaction was carried out under vigorously stirring to avoid settling of the CuO<sub>2</sub> cubes. To this purpose, the cell was mounted on a stirring plate and the solution was stirred with spherical magnetic bars.

Prior data reduction and further analysis using the Athena software,<sup>49</sup> data merging and data normalization encompassing energy calibration and alignment were performed using the Graphical User Interfaces<sup>50</sup> available at the ROCK beamline for fast and massive handling of the Quick-EXAFS data. The energy was calibrated to the first inflection point of in the derivative spectra of the respective metal foil defined at 8979 eV for Cu and at 11215 eV for Ir. Then the spectra were background corrected and normalized using NormalGui. The Cu absorption spectra were normalized using a linear function from 15 eV to 130 eV below the edge and a 2<sup>nd</sup> order polynomial function 35 eV to 800 eV above the edge, respectively. The Ir absorption spectra were normalized from 30 eV to 250 eV below the edge and 50 eV to 1480 eV above the edge, respectively. Ir L<sub>3</sub>-edge  $k^3\chi(k)$  extracted EXAFS signals were Fourier transformed in R-space pseudo radial distribution functions using a Kaiser-Bessel window between  $k_{\text{min}} = 3.0 \text{ \AA}^{-1}$  and  $k_{\text{max}} = 18 \text{ \AA}^{-1}$  and  $dk$  window sill parameter equal to 1. Cu K-edge  $k^3\chi(k)$  EXAFS signals collected were Fourier transformed in R-space pseudo radial distribution functions using a Kaiser-Bessel window between  $k_{\text{min}} = 3.0 \text{ \AA}^{-1}$  and  $k_{\text{max}} = 14.4 \text{ \AA}^{-1}$  and  $dk$  window sill parameter equal to 1. Extended X-ray Absorption Fine Structure (EXAFS) spectra were fitted using the Artemis program alternatively in  $k$  and  $R$  spaces and fitting windows are detailed in the caption below the tables.

**Multivariate Curve Resolution Analysis.** Identification of the phases present during the *in situ* treatment using time-resolved XAS studies can be obtained using the MCR-ALS (multivariate curved regression with alternative least squares fitting) chemometric method.<sup>51</sup> The MCR-ALS minimization algorithm, developed under Matlab<sup>52</sup> was used herein for isolating, from the corresponding experimental data set, the spectra of the copper and iridium intermediate species formed over the course of the reaction. This method was also used to determine the speciation of both copper and iridium species as a function of time.

## Author Contributions

ME and ADS performed material synthesis, SD and CT performed electrochemical studies, MCH and DA performed TEM characterization and analysis, SGD performed SEM experiments, VB and MG performed and analysed synchrotron experiments, JYP and JP analysed XPS and XRD results, supervised the work, and wrote the manuscript.

## Conflicts of interest

“There are no conflicts to declare”.

## Acknowledgements

Philippe Decorse is gratefully acknowledged for XPS experiments, Ivonne Cocca and Sophie Nowak for XRF measurements. We acknowledge the ITODYS XRD, XPS-UPS and SEM facilities (Université Paris Cité, CNRS UMR 7086, Paris, France). The authors acknowledge financial support from the CNRS-CEA “METSA” French network (FR CNRS 3507) on the platform of Université Paris Cité. The XAS work was supported by a public grant overseen by the French National Research Agency (ANR) as a part of the “Investissements d’Avenir” program (ref: ANR-10-EQPX-45) provided for the building of the ROCK beamline, and the Synchrotron SOLEIL proposal 20201546.

## References

1. U. Babic, M. Suermann, F. N. Büchi, L. Gubler and T. J. Schmidt, *Journal of The Electrochemical Society*, 2017, **164**, F387-F399.
2. M. Chatenet, B. G. Pollet, D. R. Dekel, F. Dionigi, J. Deseure, P. Millet, R. D. Braatz, M. Z. Bazant, M. Eikerling, I. Staffell, P. Balcombe, Y. Shao-Horn and H. Schäfer, *Chemical Society Reviews*, 2022, **21**, 4583-4762.
3. Y.-T. Kim, P. P. Lopes, S.-A. Park, A. Y. Lee, J. Lim, H. Lee, S. Back, Y. Jung, N. Danilovic, V. Stamenkovic, J. Erlebacher, J. Snyder and N. M. Markovic, *Nat. Commun.*, 2017, **8**, 1-8.
4. M. Bernicke, E. Ortel, T. Reier, A. Bergmann, J. Ferreira de Araujo, P. Strasser and R. Kraehnert, *ChemSusChem*, 2015, **8**, 1908-1915.
5. G. Ercolano, F. Farina, S. Cavaliere, D. J. Jones and J. Roziere, *Journal of Materials Chemistry A*, 2017, **5**, 3974-3980.
6. S. M. Alia, S. Pylypenko, K. C. Neyerlin, D. A. Cullen, S. S. Kocha and B. S. Pivovar, *ACS Catalysis*, 2014, **4**, 2680-2686.
7. S. M. Alia, B. A. Larsen, S. Pylypenko, D. A. Cullen, D. R. Diercks, K. C. Neyerlin, S. S. Kocha and B. S. Pivovar, *ACS Catalysis*, 2014, **4**, 1114-1119.
8. S. M. Alia, Y. S. Yan and B. S. Pivovar, *Catalysis Science & Technology*, 2014, **4**, 3589-3600.
9. J. Zheng, D. A. Cullen, R. V. Forest, J. A. Wittkopf, Z. Zhuang, W. Sheng, J. G. Chen and Y. Yan, *ACS Catalysis*, 2015, **5**, 1468-1474.
10. L. Zhang, L. T. Roling, X. Wang, M. Vara, M. Chi, J. Liu, S.-I. Choi, J. Park, J. A. Herron, Z. Xie, M. Mavrikakis and Y. Xia, *Science*, 2015, **349**, 412-416.
11. C. Chen, Y. Kang, Z. Huo, Z. Zhu, W. Huang, H. L. Xin, J. D. Snyder, D. Li, J. A. Herron, M. Mavrikakis, M. Chi, K. L. More, Y. Li, N. M. Markovic, G. A. Somorjai, P. Yang and V. R. Stamenkovic, *Science*, 2014, **343**, 1339-1343.
12. Y. Chen, F. Yang, Y. Dai, W. Wang and S. Chen, *The Journal of Physical Chemistry C*, 2008, **112**, 1645-1649.
13. X. Wang, L. Zhang, S.-I. Choi, M. Luo, L. T. Roling, J. A. Herron, M. Mavrikakis, C. Ma, M. Chi, J. Liu, Z. Xie and Y. Xia, *Nature Communications*, 2015, **6**, 7594.
14. S. Alayoglu and B. Eichhorn, *Journal of the American Chemical Society*, 2008, **130**, 17479-17486.
15. M. K. Debe, *Nature*, 2012, **486**, 43-51.
16. J. Park, T. Kwon, J. Kim, H. Jin, H. Y. Kim, B. Kim, S. H. Joo and K. Lee, *Chemical Society Reviews*, 2018, **47**, 8173-8202.
17. T. Kwon, H. Hwang, Y. J. Sa, J. Park, H. Baik, S. H. Joo and K. Lee, *Advanced Functional Materials*, 2017, **27**, 1604688.
18. H. N. Nong, H.-S. Oh, T. Reier, E. Willinger, M.-G. Willinger, V. Petkov, D. Teschner and P. Strasser, *Angewandte Chemie International Edition*, 2015, **54**, 2975-2979.
19. H. Jin, Y. Hong, J. Yoon, A. Oh, N. K. Chaudhari, H. Baik, S. H. Joo and K. Lee, *Nano Energy*, 2017, **42**, 17-25.
20. K. Sasaki, K. A. Kuttiyiel, D. Su and R. R. Adzic, *Electrocatalysis*, 2011, **2**, 134-140.
21. N. Danilovic, R. Subbaraman, K. C. Chang, S. H. Chang, Y. Kang, J. Snyder, A. P. Paulikas, D. Strmcnik, Y. T. Kim, D. Myers, V. R. Stamenkovic and N. M. Markovic, *Angewandte Chemie International Edition*, 2014, **53**, 14016-14021.
22. M. Liu, Y. Zheng, S. Xie, N. Li, N. Lu, J. Wang, M. J. Kim, L. Guo and Y. Xia, *Physical Chemistry Chemical Physics*, 2013, **15**, 11822-11829.
23. D. Yoon, S. Bang, J. Park, J. Kim, H. Baik, H. Yang and K. Lee, *CrystEngComm*, 2015, **17**, 6843-6847.
24. A. C. Foucher, S. Yang, D. J. Rosen, J. D. Lee, R. Huang, Z. Jiang, F. G. Barrera, K. Chen, G. G. Hollyer, C. M. Friend, R. J. Gorte, C. B. Murray and E. A. Stach, *Journal of the American Chemical Society*, 2022.
25. M. Elmaalouf, M. Odziomek, S. Duran, M. Gayraud, M. Bahri, C. Tard, A. Zitolo, B. Lassalle-Kaiser, J.-Y. Piquemal, O. Ersen, C. Boissière, C. Sanchez, M. Giraud, M. Faustini and J. Peron, *Nature Communications*, 2021, **12**, 3935.
26. M. Faustini, M. Giraud, D. Jones, J. Rozière, M. Dupont, T. R. Porter, S. Nowak, M. Bahri, O. Ersen, C. Sanchez, C. Boissière, C. Tard and J. Peron, *Advanced Energy Materials*, 2019, **9**, 1802136.

27. M. Odziomek, M. Bahri, C. Boissière, C. Sanchez, B. Lassalle-Kaiser, A. Zitolo, O. Ersen, S. Nowak, C. Tard, M. Giraud, F. Faustini and J. Peron, *Materials Horizons*, 2020, **7**, 541-550.
28. S. Sun and Z. Yang, *Chemical Communications*, 2014, **50**, 7403-7415.
29. Z. Wang, D. Luan, F. Y. C. Boey and X. W. D. Lou, *Journal of the American Chemical Society*, 2011, **133**, 4738-4741.
30. L. Yang, B. Zhang, W. Ma, Y. Du, X. Han and P. Xu, *Materials Chemistry Frontiers*, 2018, **2**, 1523-1528.
31. J. Nai, Y. Tian, X. Guan and L. Guo, *Journal of the American Chemical Society*, 2013, **135**, 16082-16091.
32. J. H. Sohn, H. G. Cha, C. W. Kim, D. K. Kim and Y. S. Kang, *Nanoscale*, 2013, **5**, 11227-11233.
33. B. Qiu, Q. Zhu, M. Du, L. Fan, M. Xing and J. Zhang, *Angewandte Chemie International Edition*, 2017, **56**, 2684-2688.
34. X. Guan, J. Nai, Y. Zhang, P. Wang, J. Yang, L. Zheng, J. Zhang and L. Guo, *Chemistry of Materials*, 2014, **26**, 5958-5964.
35. J. Nai, S. Wang, Y. Bai and L. Guo, *Small*, 2013, **9**, 3147-3152.
36. L. Tian, T. Yang, W. Pu and J. Zhang, *Nanoscale Research Letters*, 2019, **14**, 264.
37. Z. Wang and X. W. Lou, *Advanced Materials*, 2012, **24**, 4124-4129.
38. Y. Shang and L. Guo, *Advanced Science*, 2015, **2**, 1500140.
39. R. G. Pearson, *Journal of Chemical Education*, 1968, **45**, 581-587.
40. B. Beverskog and I. Puigdomenech, *Journal of The Electrochemical Society*, 1997, **144**, 3476-3483.
41. F. Hong, S. Sun, H. You, S. Yang, J. Fang, S. Guo, Z. Yang, B. Ding and X. Song, *Crystal Growth & Design*, 2011, **11**, 3694-3697.
42. A. Minguzzi, C. Locatelli, O. Lugaresi, E. Achilli, G. Cappelletti, M. Scavini, M. Coduri, P. Masala, B. Sacchi, A. Vertova, P. Ghigna and S. Rondinini, *ACS Catalysis*, 2015, **5**, 5104-5115.
43. V. Pfeifer, T. E. Jones, J. J. Velasco Velez, R. Arrigo, S. Piccinin, M. Havecker, A. Knop-Gericke and R. Schlögl, *Chemical Science*, 2017, **8**, 2143-2149.
44. H. Jang and J. Lee, *Journal of Energy Chemistry*, 2020, **46**, 152-172.
45. P. M. Diehm, P. Ágoston and K. Albe, *ChemPhysChem*, 2012, **13**, 2443-2454.
46. S. Duran, M. Elmaalouf, M. Odziomek, J.-Y. Piquemal, M. Faustini, M. Giraud, J. Peron and C. Tard, *ChemElectroChem*, 2021, **8**, 3519-3524.
47. L. Lutterotti, S. Matthies and H.-R. Wenk, *IUCr: Newsletter of the CPD*, 1999, **21**, 14-15.
48. V. Briois, C. La Fontaine, S. Belin, L. Barthe, T. Moreno, V. Pinty, A. Carcy, R. Girardot and E. Fonda, *Journal of Physics: Conference Series*, 2016, **712**, 012149.
49. B. Ravel and M. Newville, *Journal of Synchrotron Radiation*, 2005, **12**, 537-541.
50. C. Lesage, E. Devers, C. Legens, G. Fernandes, O. Roudenko and V. Briois, *Catalysis Today*, 2019, **336**, 63-73.
51. W. H. Cassinelli, L. Martins, A. R. Passos, S. H. Pulcinelli, C. V. Santilli, A. Rochet and V. Briois, *Catalysis Today*, 2014, **229**, 114-122.
52. J. Jaumot, R. Gargallo, A. de Juan and R. Tauler, *Chemometrics and Intelligent Laboratory Systems*, 2005, **76**, 101-110.